

Article

Incorporation of Manganese (II) in Beta-Tricalcium Phosphate from EPR and ENDOR Measurements for Powders

Fadis F. Murzakhanov ^{1,*} , Anna A. Forsyenkova ², Inna V. Fadeeva ², Georgy V. Mamin ¹ 
and Marat R. Gafurov ¹ 

¹ Institute of Physics, Kazan Federal University, Kremlevskaya 18, 420008 Kazan, Russia; georgemamin@gmail.com (G.V.M.); marat.gafurov@kpfu.ru (M.R.G.)

² A.A. Baikov Institute of Metallurgy and Material Science, Russian Academy of Sciences, Leninsky Prospekt 49, 119334 Moscow, Russia; aforysenkova@gmail.com (A.A.F.); fadeeva_inna@mail.ru (I.V.F.)

* Correspondence: murzakhanov.fadis@yandex.ru; Tel.: +7-9270395512

Abstract: Powders of β -tricalcium phosphate (β -TCP, Ca_3PO_4) doped with manganese (Mn^{2+}) are comprehensively analyzed with electron paramagnetic resonance (EPR) and electron-nuclear double resonance (ENDOR) techniques. The modeling of the spectra permitted to calculate the values of zero-field splitting ($B_2^0 = -904$ MHz; $B_4^0 = -1.41$ MHz and $B_4^3 = 195.2$ MHz) and explain the origin of the low-field hyperfine structures as the allowed spin transitions of fine structure. Three structurally inequivalent positions for Mn^{2+} in the β -TCP crystal lattice are identified and their g -factors and hyperfine constants are quantified. The obtained results can serve as fundamental background to the study of structurally disordered matrices with high spin ($S \geq 1$) impurities which are important for catalytic systems.

Keywords: tricalcium phosphate; manganese; ceramics; catalyst; electron paramagnetic resonance



Citation: Murzakhanov, F.F.; Forsyenkova, A.A.; Fadeeva, I.V.; Mamin, G.V.; Gafurov, M.R. Incorporation of Manganese (II) in Beta-Tricalcium Phosphate from EPR and ENDOR Measurements for Powders. *Ceramics* **2022**, *5*, 318–329. <https://doi.org/10.3390/ceramics5030025>

Academic Editor: Jose M.F. Ferreira

Received: 27 June 2022

Accepted: 22 July 2022

Published: 26 July 2022

Publisher's Note: MDPI stays neutral with regard to jurisdictional claims in published maps and institutional affiliations.



Copyright: © 2022 by the authors. Licensee MDPI, Basel, Switzerland. This article is an open access article distributed under the terms and conditions of the Creative Commons Attribution (CC BY) license (<https://creativecommons.org/licenses/by/4.0/>).

1. Introduction

Transition metal catalysts are used in pharmaceuticals, in the production of natural products, chemistry, the hydrogenation of aromatic hydrocarbons, heavy-oil upgrading, etc. [1–5]. Key to the catalytic importance of transition metals is the presence of partially filled d shells (unpaired electrons) leading to the appearance of paramagnetism. The complex ligand structure that surrounds the catalyst's central active site has a great influence in controlling the activity, selectivity and specificity of the catalyst and even subtle changes in the first and following coordination spheres deserve a thorough investigation [6].

Electron paramagnetic resonance (EPR) has found wide use in identification of the intermediate compounds and revelation of the correlation between the structural details and activity of the systems. High sensitivity of the EPR method and its selectivity to the paramagnetic compounds set the stage for the study of the intermediates containing unpaired electrons directly in the catalytic systems, even without their isolation from solutions, i.e., so even in conditions extremely like those occurring in a real catalytic reactor [7–12].

This potential is nowadays enormously extended thanks to the availability of high-field and advanced pulsed methods. These high-resolution techniques allow resolving weak magnetic interactions, not usually resolved in conventional continuous wave (cw) EPR experiments. In particular, electron-nuclear double resonance (ENDOR) allows detecting the nuclear magnetic resonance (NMR) transition frequencies of nuclei coupled to unpaired electrons, providing unique information in both the local structure and the nature of the chemical bond between the metal center and the surrounding ligands [13,14].

Calcium phosphates (CaP) based materials are used and developed not only for biomedical purposes [15–18] but also as catalysts' support [19]. CaP contains Ca^{2+} cations together with orthophosphate (PO_4^{3-}), metaphosphate (PO_3^-), or pyrophosphate ($\text{P}_2\text{O}_4^{7-}$) anions, and sometimes hydrogen (H^+) or hydroxide (OH^-) ions. Calcium phosphates with

a Ca/P ratio in the range of 1.5 and 1.67 are called apatites [16]. Among the apatites, hydroxyapatite ($\text{Ca}_{10}(\text{PO}_4)_6(\text{OH})_2$, HAp) is the most famous one used as heterogeneous catalysts [20–22]. The hydroxyapatite materials were more effective at coupling and dehydrogenation compared to calcium oxide. Other representatives of the large CaP family are studied much less, although tricalcium phosphate (TCP, Ca_3PO_4) showed a higher rate of alcohol coupling compared with the hydroxyapatite (see, for example [23,24]). β -TCP structures attract attention because of their ability to demonstrate not only catalytical but also non-linear optical, ferroelectric, antiferroelectric, and bioregenerative properties. Such a wide field of possible applications of these materials is due to the unique structure of β -TCP in comparison with other CaPs [25].

β -TCP is characterized by a rhombohedral structure with the space group $R3c$ and five inequivalent Ca sites (Figure 1) with coordination numbers ranging from six to nine and various Ca–O distances offering a wide range of cationic substitutions. It is usually assumed that the cation site affinity is ruled by steric criteria (rather than by charge) [26] meaning that for example Zn^{2+} , Mn^{2+} ions (with cationic radii smaller than 1.1 Å) incorporates mainly in Ca5 sites [27,28] or fully Ca3 if their radii are larger than 1.3 Å like Sr^{2+} or Ba^{2+} .

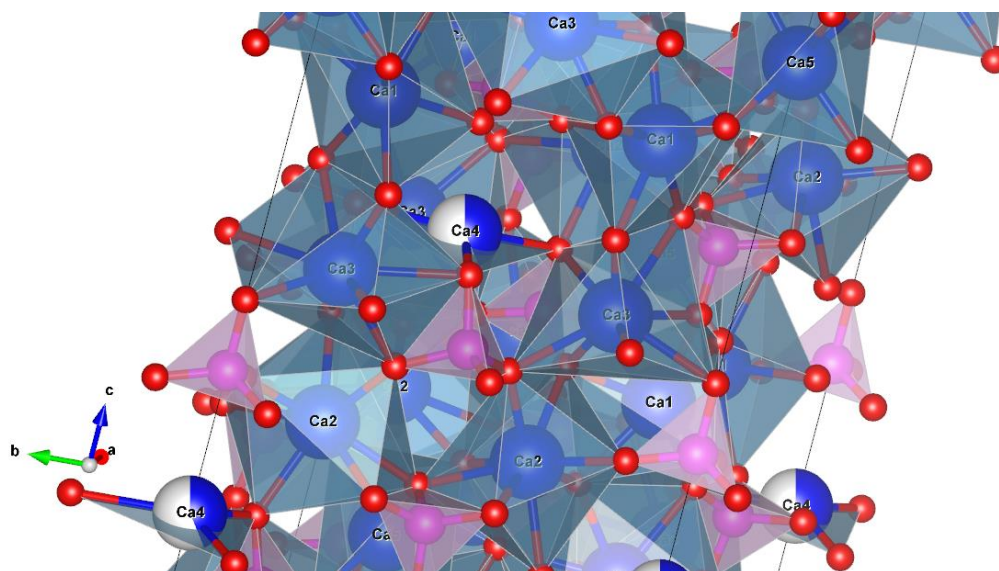


Figure 1. β -TCP crystal structure with the corresponding calcium and phosphorus polyhedra, where red balls—oxygen, blue—calcium, pink—phosphorus.

As concerning transition metals, manganese is one of the commonly used dopant and metal centers for various types of catalysts including hydroxyapatites [29–32]. In a recent investigation [33], Mn-doped α -tricalcium phosphate was extensively studied. In paper [34] bioactive manganese-doped TCP/HA ceramic coatings were developed. It was shown that Mn ions in the TCP structure were present in both Mn^{2+} and Mn^{3+} oxidation states and manganese clusters were revealed.

The incorporation of Mn into the HAp crystal structure has been extensively investigated by various methods including EPR (see [35,36] and references therein). It was shown that in HAp (in contrast to the steric rule) both Ca1 and Ca2 sites are occupied by Mn^{2+} even at a low manganese concentration. It is logical to assume that for the β -TCP not only Ca5 sites as mentioned above can be filled but (at least for some of the synthesis conditions or manganese concentrations) also other calcium positions. Due to the structure complexity, in comparison with HAp, there are not many experimental, theoretical, and computational studies of TCP doping. Some reliable analytical approach(es) should be introduced and applied to unravel the dopant positions. EPR techniques can help to get the required information [37,38].

Interpretation of the EPR spectra for the transition metal ions is often complicated due to their high electron spin (S). The spin systems with $S = 2$ (quintet) and $S = 5/2$ (sxtet)

can experience fourth-order zero field interaction terms. On the contrary to the quintet, the $S = 5/2$, fourth-order zero-field splitting (ZFS) is much more easily determined since it may be the only ZFS possible in the spherically symmetric high-spin d^5 configuration. The common axial symmetry situation, where ZFS predominates by second-order terms (i.e., D), the zero-field energies facilitate as follows: $E_{1,2} = -8/3 \times D$; $E_{3,4} = -2/3 \times D$; $E_{5,6} = +10/3 \times D$. These expressions give relative energies of 0, 2D, and 4D and correspond to the three Kramers doublets, accordingly, $|5/2, \pm 5/2\rangle$, $|5/2, \pm 3/2\rangle$, $|5/2, \pm 1/2\rangle$ [39]. The presence of a gradient crystal field leads to the appearance of five fine structure components, that are usually described by axial spin-Hamiltonian with D and E in powder systems [40]. However, this is not enough to describe satisfactorily the low-field lines arising from the high-order zero splitting components. Additionally, the mixing of spin sublevels leads to an extremely complex angular dependence of each component of the fine structure.

The aim of the present work was to develop the EPR-based approaches for the study of the influence of manganese doping on the structure of β -TCP and to give a reasonable explanation for the observed powders' spectral features.

2. Materials and Methods

Calcium nitrate tetrahydrate ($\text{Ca}(\text{NO}_3)_2 \cdot 4\text{H}_2\text{O}$, $\geq 99\%$, Reakhim, Russian Federation), manganese(II) acetate ($\text{Mn}(\text{CH}_3\text{COO})_2$, $\geq 98\%$, Reakhim, Russian Federation) and diammonium hydrogen phosphate ($(\text{NH}_4)_2\text{HPO}_4$, $\geq 98\%$, Reakhim, Russian Federation) were used as starting materials for the synthesis. The synthesis was carried out at room temperature, of about 25 °C. The synthesis of Mn-doped TCP proceeded as follows. First, calcium nitrate and manganese acetate were dissolved in deionized water at the total metal ion concentration of 0.5 M, after which an appropriate amount of 0.5 M $(\text{NH}_4)_2\text{HPO}_4$ solution was added dropwise under vigorous stirring for 30 min, while manually controlling the pH to around 6.5 by the addition of concentrated ammonia (NH_4OH , 25%, Reakhim, Russian Federation). The total metal ion to phosphorous ratio was kept at 1.50 for all the synthesized compounds. The obtained precipitates were mixed in the reaction mixture for 30 min after the addition of $(\text{NH}_4)_2\text{HPO}_4$ and afterwards filtered, washed with deionized water and dried at 110 °C overnight in the oven. Finally, dry powders were ground in an agate mortar and annealed in the air atmosphere at 400 °C and 900 °C for 2 h, with the heating rate of 10 °C/min. Four samples were synthesized, containing different Mn^{2+} contents: TCP, 0.1MnTCP, 0.01MnTCP, and 0.001MnTCP. With this denotation, 0.01MnTCP, for example, means that 0.01 mol.% of Mn^{2+} is estimated to have been incorporated in the TCP structure based on precursor concentrations, yielding the molecular formula $\text{Mn}_{0.01}\text{Ca}_{2.99}(\text{PO}_4)_2$. The corresponding stoichiometries of TCP, 0.1MnTCP and 0.001MnTCP equaled $\text{Ca}_3(\text{PO}_4)_2$, $\text{Mn}_{0.1}\text{Ca}_{2.90}(\text{PO}_4)_2$ and $\text{Mn}_{0.001}\text{Ca}_{2.999}(\text{PO}_4)_2$, respectively. Detailed characterizations of the samples by various analytical techniques are given in paper [41].

EPR measurements were performed using the W-band (with the microwave frequency of $\nu_{\text{MW}} \approx 93.5$ GHz) Bruker Elexsys E680 and the X-band ($\nu_{\text{MW}} \approx 9.5$ GHz) Bruker Elexsys E580 spectrometers (Germany, Karlsruhe) both in conventional (cw) and pulsed modes. While cw EPR uses continuous microwave irradiation and reveals splitting of energy levels of paramagnetic system, pulse techniques provide insights into the dynamics of the system and allow one to measure relaxation times—longitudinal or spin-lattice relaxation time T_1 and transverse or spin-spin relaxation time T_2 . The typical pulse sequences we used in our research in the X and W-band were: (1) $\pi/2 - \tau - \pi$ with the $\pi/2$ pulse duration of 32 ns and the time delay $\tau = 240$ ns to obtain electron spin echo (ESE); (2) T_2 was measured by tracking the primary ESE amplitude with the same $\pi/2 - \pi$ pulse durations while varying τ ; (3) T_1 was extracted from the inversion-recovery studies by applying the $\pi - T_{\text{delay}} - \pi/2 - \tau - \pi$ pulse sequence, while T_{delay} was varied.

For ENDOR experiments we used special (for nuclei and electron) cavities and applied Mims pulse sequence $\pi/2 - \tau - \pi/2 - T - \pi/2$ with an additional radiofrequency (RF) pulse with the frequency swept in the range of 1–200 MHz inserted between the second

and third microwave $\pi/2$ pulses. Details of ENDOR experiments and their interpretation for studying CaP systems are given in [42].

EPR analysis and simulation of angular dependence of the zero-field splittings were conducted using Matlab 2018b with the Easyspin software package [43].

3. Results and Discussion

3.1. X-Band Measurements

The EPR spectra of TCP-Mn in both cw and pulsed modes at X-band are depicted in Figure 2. ESE was not observed at room temperature due to the short relaxation times, so the further experiments using pulsed mode were conducted at $T = 50$ K. At higher manganese concentrations ($x = 0.1$), the EPR signal in the pulsed mode was not observed for T down to 10 K due to the very short value of T_2 with the corresponding line broadening (loss of the information about the hyperfine structure). The T_2 value specifies the relaxation (recovery) rate of the spin system from their excited state due to the spin-spin interaction between equivalent paramagnetic centers.

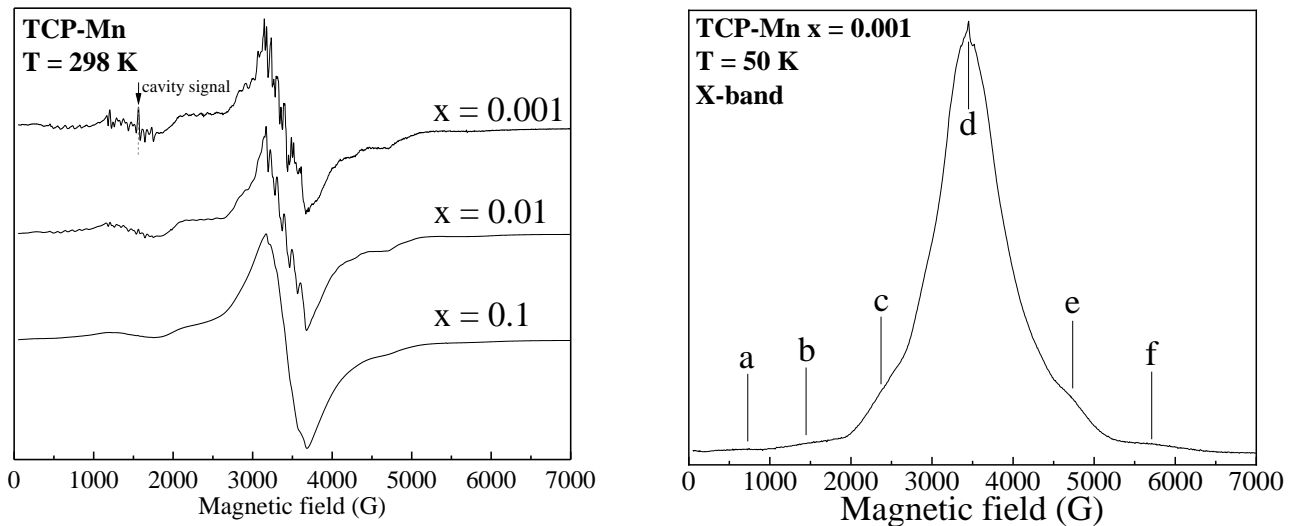


Figure 2. cw EPR at room temperature depending on the concentration of manganese ions embedded in the structure (**left panel**). ESE EPR for 0.001MnTCP; (a–f) denote the components of a fine structure (**right panel**).

The relaxation time measurements give the same values of T_1 ($\approx 1.5 \mu\text{s}$) and T_2 ($\approx 105 \mu\text{s}$) as measured throughout the magnetic field (H_0 or B_0) and range from 50 G to 7000 G. The T_1 time indicates the spin-lattice relaxation rate owing to the interaction between longitudinal magnetization of Mn^{2+} ions and the crystal lattice (matrix) of TCP. The absence of any drastically changes of the relaxation times with B and roughly monoexponential types of T_1 and T_2 curves allows one to assume that uncontrolled manganese phases were not formed during the synthesis, which would contribute to the appearance of additional signals in both the cw and ESE spectra (cf. with [44], for example).

To describe the obtained EPR spectra we used the following spin Hamiltonian from the crystal field theory [35]:

$$\hat{H} = g\beta H_0 \hat{S}_z + B_2^0 O_2^0 + B_4^0 O_4^0 + B_4^3 O_4^3 + A_{iso} (\hat{S}_z \hat{I}_z) \quad (1)$$

where the first term is Zeeman interactions (Z_e), second, third and fourth are responsible for the fine structure and ZFS, and the fifth one is hyperfine splitting (hfs). Here $B_k^q = c_k^q \cdot b_k^q$ are the parameters of the electric crystal field (for example $c_2^0(\theta, \varphi) = 3\cos^2(\theta) - 1$ and $c_2^2(\theta, \varphi) = \cos^2(\varphi) - \sin^2(\varphi)$), b_k^q -crystal field values. O_k^q are the Stevens operators (for example $O_2^0 = 3S_z^2 - S(S+1)$ and $O_2^2 = S_x^2 - S_y^2$). The maximum power is determined by the value of the spin number since the restrictions are: $k \leq 2$ for

$S = 1$ and $3/2$, $k \leq 4$ for $S = 2$ and $5/2$, $k \leq 6$ for $S = 3$ and $7/2$, where only even terms ($k = 0, 2, 4$ and 6) can contribute. The value of q is equal to the multiplicity of the symmetry of the crystal lattice. Stevens operators are known, while the parameters of the crystal field depend on the environment of the impurity ion. Note that g -factor and A_{iso} —constant of hyperfine interaction are assumed to be isotropic values. As seen from (1), the EPR spectra are due to ZFS of the ${}^6S_{5/2}$ ground state electron spin $S = 5/2$, and hyperfine coupling to the ${}^{55}\text{Mn}$ nuclear spin (100% abundance) with $I = 5/2$ [33].

The main reason for using such spin Hamiltonian is to observe several hfs in powder spectra. The low-field hfs (so called singularity signals) observed in the experiments evoke a particular interest for their study (Figure 3). In orientationally-disordered environments (e.g., powder samples) observation of allowed non-central transitions is extremely rare from an experimental point of view. Therefore, the low-field spectral features are analyzed in detail below.

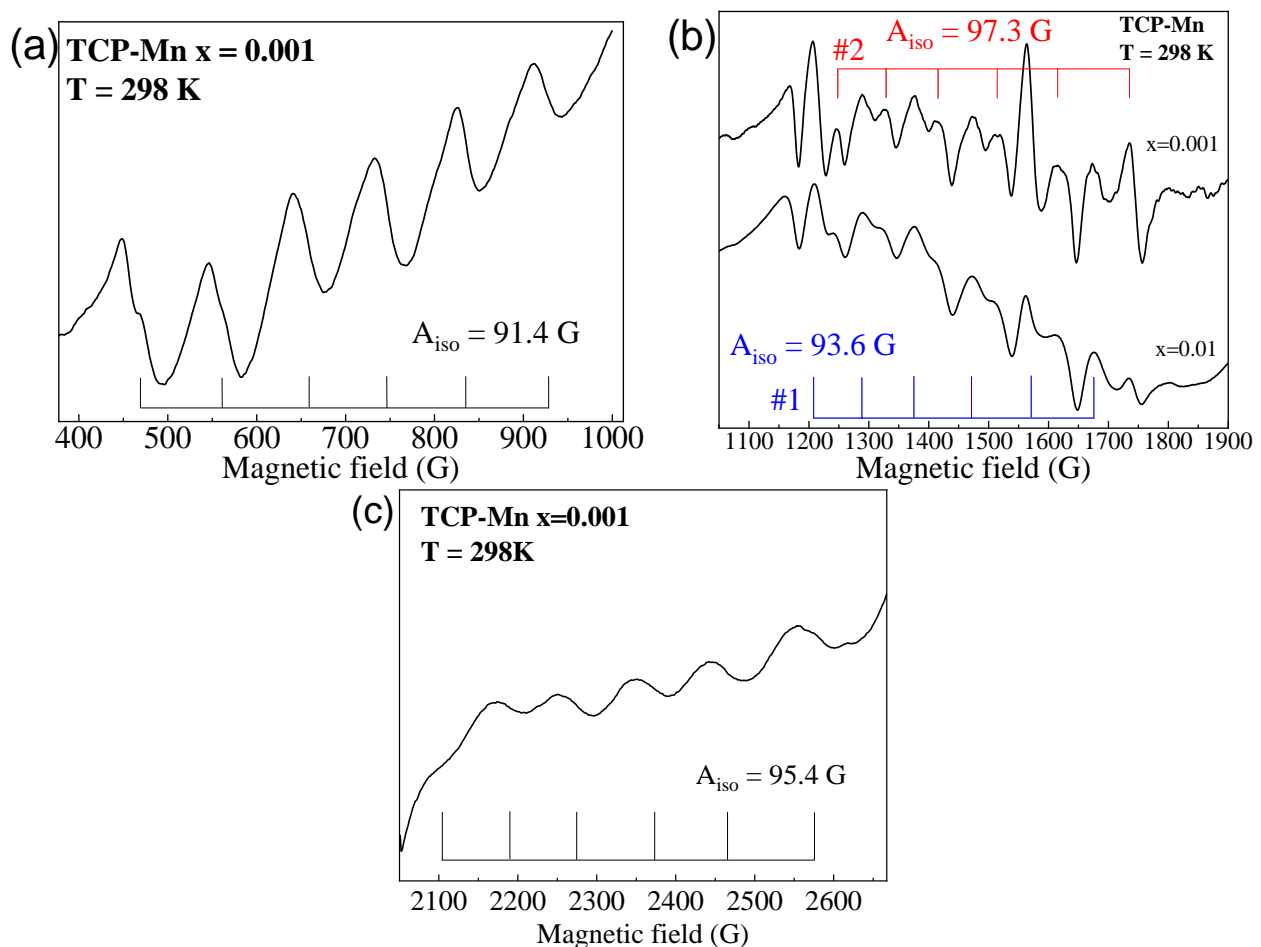


Figure 3. Low field components of the fine structure with 6 splittings of isotropic hyperfine interaction for 0.001MnTCP at three ranges of magnetic field sweeping corresponding to the (a) $|+5/2\rangle \rightarrow |+3/2\rangle$ spin transition for parallel orientation with $B_{res1} = 688$ G, (b) $|+3/2\rangle \rightarrow |+1/2\rangle$ spin transition for perpendicular orientation with $B_{res2} = 1400$ G and (c) $|+3/2\rangle \rightarrow |+1/2\rangle$ spin transition for parallel orientation with $B_{res3} = 2330$ G.

We suppose that these singularities belong to the transitions of non-central (low-field) components of the fine-structure in accordance with the selection rules (Figure 4, left panel). Nanocrystals oriented in the proximity of canonical positions give the main contribution to these signals. The presented theoretical calculation (Figure 4, right panel) of resonance transition values and construction of the angular dependence model of the fine-structure components using correct spin Hamiltonian, confirm our assumptions. The theoretical

model of orientation dependence of ZFS components clearly demonstrate that there are several resonance lines at low magnetic field which weakly depend on orientation. The excellent agreement between calculated and experimental data demonstrates that using correct spin Hamiltonian allow one to describe and explain the nature of the low-field (LF) spectral features.

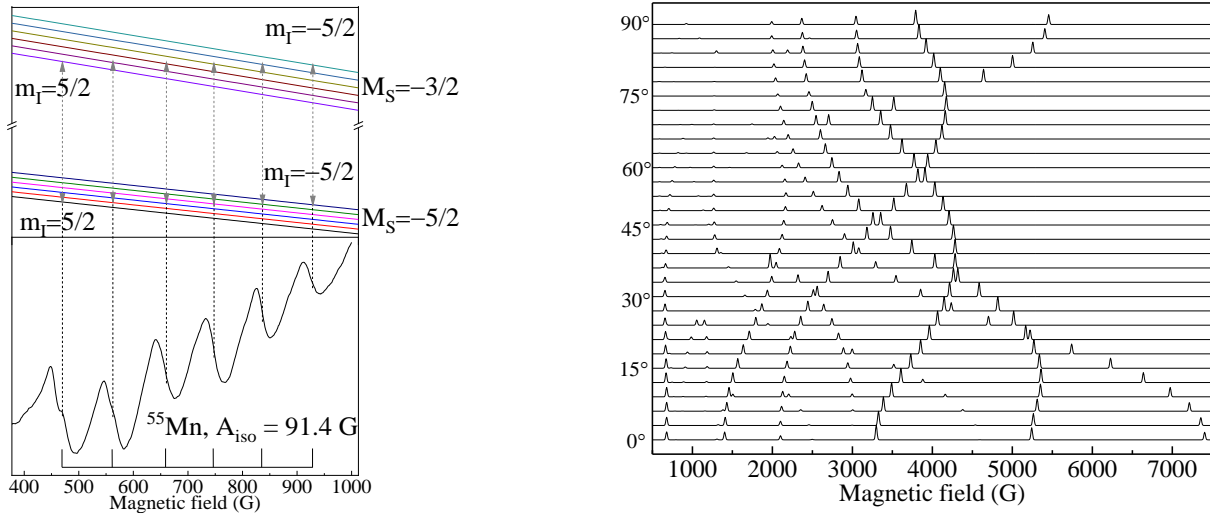


Figure 4. The scheme of hyperfine interaction levels and the nature of the formation of 6 lines due to the allowed spin transitions $\Delta M_S = -3/2 - 5/2$ and $m_I = 5/2$ (left panel). A theoretical model of the angular dependence of fine structure components for Mn^{2+} ions in a TCP sample (right panel).

To determine the parameters of the ZFS (B_2^0 , B_4^0 and B_4^3) it was assumed that the low-field signals refer to the allowed transitions of the ZFS at the canonical orientation (parallel position of the nanocrystal relative to the external magnetic field B_0). Then, through the spin Hamiltonian and the corresponding wave functions, for each magnetic resonance absorption line equation was calculated that includes itself the parameters of ZFS.

$$\begin{aligned}
 E_1 |M_S = \frac{5}{2}\rangle &= \frac{5}{2}Z_e + 10B_2^0 + 60B_4^0 \\
 E_2 |M_S = \frac{3}{2}\rangle &= \frac{3}{2}Z_e - 2B_2^0 - 180B_4^0 \\
 E_3 |M_S = \frac{1}{2}\rangle &= \frac{1}{2}Z_e - 8B_2^0 + 120B_4^0 \\
 E_4 |M_S = -\frac{1}{2}\rangle &= -\frac{1}{2}Z_e - 8B_2^0 + 120B_4^0 \\
 E_5 |M_S = -\frac{3}{2}\rangle &= -\frac{3}{2}Z_e - 2B_2^0 - 180B_4^0 \\
 E_6 |M_S = -\frac{5}{2}\rangle &= -\frac{5}{2}Z_e + 10B_2^0 + 60B_4^0
 \end{aligned}$$

EPR transitions:

$$\begin{aligned}
 E_1 - E_2 &= Z_e + 12B_2^0 + 240B_4^0 = h\nu \text{ (LF transition)} \\
 E_2 - E_3 &= Z_e + 6B_2^0 - 300B_4^0 = h\nu \text{ (LF transition)} \\
 E_3 - E_4 &= Z_e = h\nu \text{ (central transition)} \\
 E_4 - E_5 &= Z_e - 6B_2^0 + 300B_4^0 = h\nu \\
 E_5 - E_6 &= Z_e - 12B_2^0 - 240B_4^0 = h\nu \\
 \Delta_1 &= B_{res2} - B_{res1} = 6B_2^0 + 540B_4^0 \\
 \Delta_2 &= B_{res3} - B_{res2} = 6B_2^0 - 300B_4^0 \\
 \Delta_1 - \Delta_2 &= 840B_4^0 \\
 B_4^0 &= \frac{\Delta_1 - \Delta_2}{840} \\
 B_2^0 &= \frac{\Delta_1 - 540B_4^0}{6}
 \end{aligned}$$

where $B_{res1} = 688$ G, $B_{res2} = 1400$ G, $B_{res3} = 2330$ G, $h\nu$ —energy of the microwave quant. The magnitudes of the magnetic field have been determined from the experiment. Consequently, unknown values of ZFS were found by means of solving the equations. At

the last step to determine these values a simulation of the angular dependence model more accurately, the MATLAB was used. The results obtained are given in Table 1.

Table 1. The spin-Hamiltonian parameters of zero-field splitting for Mn^{2+} ions in TCP.

B_2^0	B_4^0	B_4^3
−904 MHz	−1.41 MHz	195.2 MHz

Accordingly, the low-field hfs can be interpreted as spin transitions which satisfy selection rules $\Delta M_S = \pm 1$, $\Delta m_I = 0$. Otherwise, if spin transitions correspond to the change of quantum spin number by $\Delta M_S = \pm 2, \pm 3$, the constant of hfs must be equal to $2 \times A_{iso}$ (so called forbidden transitions).

It is worth noting that an additional splitting of the low-field hfs onto two components can be observed (cf. Figure 3b). Each component equally increases in intensity with the increasing concentration of impurity ions. It gives a sign that the manganese ion occupies several (at least two) of the five possible, structurally nonequivalent positions (cf. Figure 1) already at very low concentrations of $x = 0.001$, with further equally probable filling. We excluded that an anisotropy of hyperfine interaction could be responsible for the observed effect—such splitting should be observed for other spin transitions of a fine structure too and attempts to simulate only this section of the EPR spectrum with anisotropic hfs parameters also failing. For a more comprehensive analysis, the additional measurements were performed in the high-frequency (HF) range of experimental setup.

3.2. High Frequency EPR Spectroscopy

The important advantage of HF-EPR used in this work is the higher spectral resolution, which allows one to distinguish the paramagnetic centers with slight variations of their g -factors. The temperature has been reduced to 50 K to improve the signal-to-noise ratio (Figure 5). The appearance of the observed structure in the vicinity of $g = 2$ is due to the hfs of Mn^{2+} ions. As seen, the EPR signal consists of three different superimposed hyperfine structures. Each of these hyperfine structures has its own set of spectroscopic parameters, as listed in Table 2. We assume that this EPR pattern is due to three different Mn^{2+} positions in the structure of the sample under study. Each of these nonequivalent positions has a different ionic environment with corresponding symmetry which affects the g -factor and hfs constant.

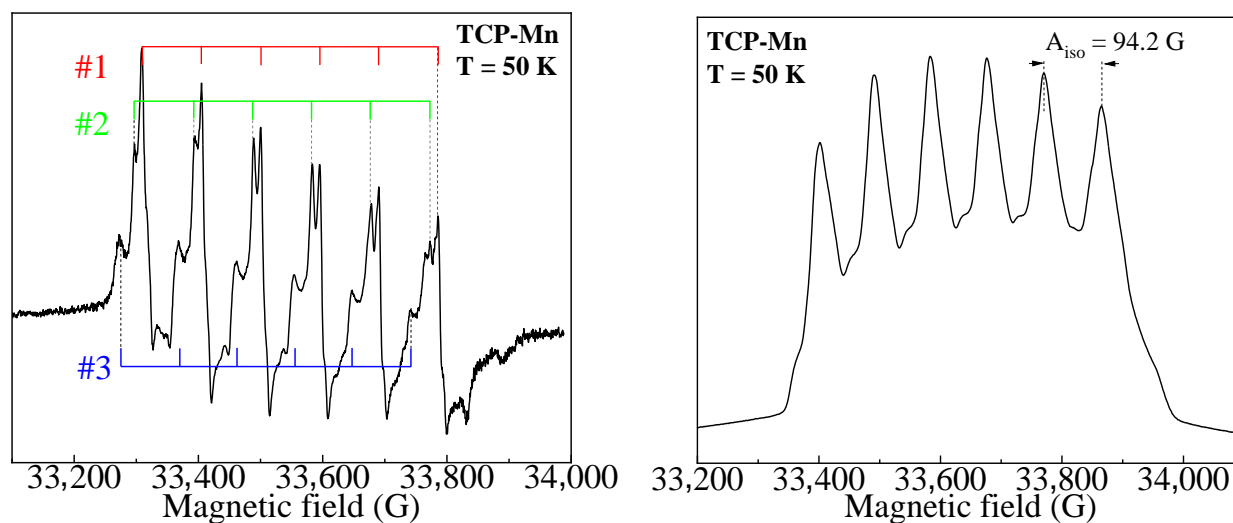


Figure 5. Spectra of high-frequency EPR of hyperfine interaction for the central transition of the fine structure of manganese for 0.001MnTCP in cw (left panel) and ESE (right panel) modes.

Table 2. The main spectroscopic and relaxation characteristics of Mn^{2+} ions in TCP for 0.001MnTCP extracted at $T = 50$ K. The relaxation times were measured as a functions of magnetic field B_0 from 33,380 G to 34,000 G.

<i>g</i> -Factor	A_{iso} (G)	Linewidth (G)	T_1 (μ s)	T_2 (μ s)
2.0040(5)	95.4(2)	9(1)	97(1)	1.51(3)
2.0055(5)	95.2(2)	12(1)	101(1)	1.49(3)
2.0080(5)	93.7(3)	18(2)	109(2)	1.5(3)

An HF-EPR spectrum in the larger magnetic fields sweep range is shown in Figure 6. It can be noted that each hyperfine component of total signal in pulse mode (Figure 5 right panel) at central transition has a triangular shaped line, caused by the overlapping signals of three manganese positions with each other. Measurements of the relaxation time obtained as a function of the external magnetic field B_0 from 33,380 G to 34,000 G demonstrate the presence of three different values of T_1 . This can serve as additional argument supporting the assumption of three nonequivalent positions of manganese, because the values of T_1 depend on the local environment (symmetry). It is hardly to assume that the existence of several EPR components (or hyperfine structures) could be due to the presence of other manganese-containing phases (hydroxyapatite or octacalcium phosphate). In this case, the relaxation times would differ by an order of magnitude, see [44], for example.

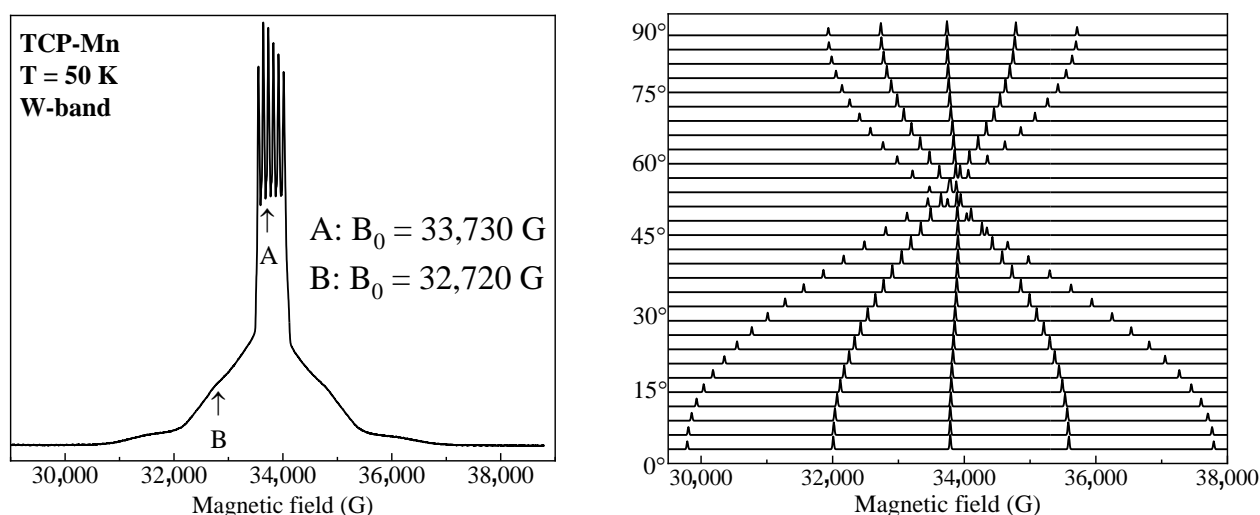


Figure 6. ESE HF-EPR for 0.001MnTCP with registration of all components of the fine structure (left panel). Theoretical model of the angular dependence of the components of a fine structure in the W-band (right panel).

Additional measurements were carried out in a wide range of magnetic fields (from 50 mT to 3.5 T, or from 500 G to 35,000 G) to confirm the absence of other EPR signals at low fields (such as in the vicinity of $g \approx 9.7$, $g \approx 4.3$). This serves as additional argument in favor of the fact that the wide EPR signal obtained belongs to the allowed transitions of the fine-structure of the Mn^{2+} ions with $g \approx 2$. The presented model of the orientation dependence of the fine structure components in the W-band with the same parameters as for the X-band, is shown in Figure 6. It is simpler than in the X-band (cf. Figure 4) due to the fact that with the increase of the magnetic field strength by 10 times, the wave functions became more “pure”. This also explains appearance of the hfs at the central transition of the EPR spectrum, since the central component of the fine structure has become less dependent on the orientation.

3.3. ENDOR Measurements

The crystal lattice of TCP contains an ion with a magnetic nuclear moment ^{31}P (100% abundance) with nuclear spin $I = 1/2$. Figure 7 shows the obtained HF ENDOR spectrum using the Mims pulse sequence for two different values of external magnetic field. Three resolved superhyperfine splittings are observed, with their own splitting values caused by the $^{31}\text{P}\text{-Mn}^{2+}$ nuclear-electron interaction. These constants depend on the distance between interacting ions. Three different values of splitting are excellent evidence for the assumption of three nonequivalent positions of manganese. This is justified by the fact that each Ca position in the structure of TCP has a different interatomic distance to phosphorus [45]. Probably, the difference in the linewidth of each splitting is due to a different scatter of lengths between specific (distinct) positions of manganese substituting the Ca site and coordination spheres of phosphorus. In addition, one of the possible reasons is associated with dipole-dipole broadening due to the powder averaging.

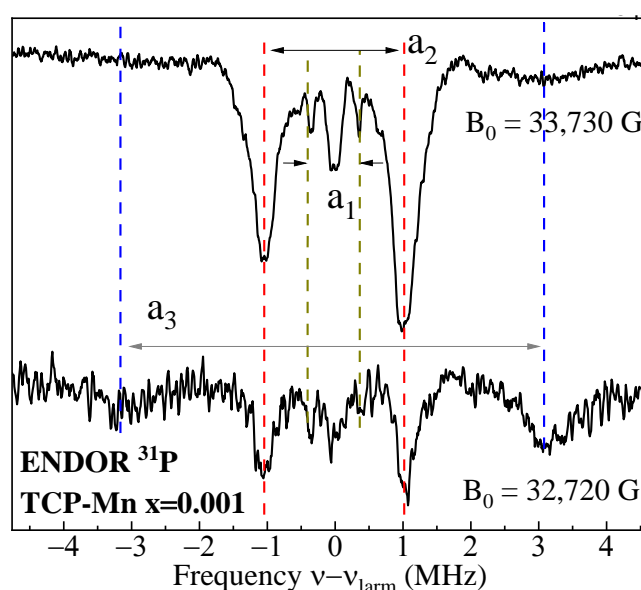


Figure 7. ^{31}P ENDOR spectrum for 0.001MnTCP (in the region of the Larmor frequency of ^{31}P). The observed splittings indicate the presence of several positions of Mn^{2+} ions in the crystal lattice of TCP. The hyperfine values are $a_1 = 0.7$ MHz, $a_2 = 2.05$ MHz and $a_3 = 6.4$ MHz.

The hyperfine structure constants containing two different contributions related to dipole-dipole interaction (anisotropic part) and to Fermi contact interaction (isotropic part) were used to estimate the interatomic distance between Mn and ^{31}P . In point dipole approximation the distance can be estimated as 3–4 Å. The intensity redistribution depending on a fixed external magnetic field is caused by angular dependence of the splitting value related to anisotropic dipole-dipole interaction. In addition, manganese has a weak spatial electron density distribution on phosphorus nuclei, since all the electron density is concentrated on the ion itself. Thus, the contribution of Fermi contact interaction is negligibly small and is not considered in calculations.

The integral intensity of each structure is directly related to the number of phosphorus ion nuclei on the particular coordination sphere. Consequently, using the relation of the integral intensities' values of splittings with each other comparing with the relative number of nuclei on the different coordination phosphorus spheres positions of manganese can approximately be defined. We assume that manganese has occupied three specific positions of calcium. The two main arguments of this assumption are the number of phosphorus nuclei surrounded by each position, which corresponds to the intensity of ENDOR spectra and calculated distance (in dipole-dipole approximation) to these nuclei which has good agreement with interatomic length data obtained from the x-ray measurements [41]. The powder form of the samples leads to additional difficulties and restrictions during the in-

terpretation of experimental results. Therefore, the results concerning manganese positions have a probabilistic character and require further additional investigation by, for example, the DFT calculations approach for refinements contributions to hfs value. Thus, these experimental datasets are an excellent reference point for further research of the relevant materials from calcium phosphate groups.

4. Conclusions

The structural and fundamental features of the spin system of TCP-Mn were analyzed by the electron paramagnetic resonance and electron-nuclear double resonance techniques. A comprehensive study by multifrequency and pulse approaches made it possible to identify the presence of three structurally unequal positions of manganese ions in the crystal lattice of the sample. The main spin-Hamiltonian parameters (g-factors, zero-field splitting and hyperfine constant) with dynamic (T_1 and T_2 relaxation) characteristics were precisely determined for each Mn^{2+} center. The modeling of the EPR spectra permitted us to calculate the high order term values of zero-field splitting ($B_2^0 = -904$ MHz; $B_4^0 = -1.41$ MHz and $B_4^3 = 195.2$ MHz) for powder systems and explain the origin of low-field hyperfine structures as the allowed spin transitions of a fine structure. The obtained results can be served as a fundamental background to the study of structurally disordered matrices with high spin impurities ($S \geq 1$) and have additionally applied importance in the chemical synthesis field or clinical industry.

Author Contributions: The research work was performed and completed through the contributions of all authors. F.F.M. and M.R.G. designed and administered the experiments. A.A.F. and I.V.F. synthesized the samples. F.F.M. and G.V.M. conducted all EPR experiments. F.F.M. and M.R.G. wrote the draft of the manuscript. All authors analyzed and discussed the data. All authors have read and agreed to the published version of the manuscript.

Funding: RSF grant #21-73-30023.

Institutional Review Board Statement: Not applicable.

Informed Consent Statement: Not applicable.

Data Availability Statement: Data can be available upon request from the authors.

Conflicts of Interest: The authors declare no conflict of interest.

References

1. Makshakova, O.N.; Shurtakova, D.V.; Vakhin, A.V.; Grishin, P.O.; Gafurov, M.R. Incorporation of iron(II) and (III) in hydroxyapatite—A theoretical study. *Crystals* **2021**, *11*, 1219. [[CrossRef](#)]
2. Nie, R.; Tao, Y.; Nie, Y.; Lu, T.; Wang, J.; Zhang, Y.; Lu, X.; Xu, C.C. Recent advances in catalytic transfer hydrogenation with formic acid over heterogeneous transition metal catalysts. *ACS Catal.* **2021**, *11*, 1071–1095. [[CrossRef](#)]
3. Kosinov, N.; Liu, C.; Hensen, E.J.M.; Pidko, E.A. Engineering of transition metal catalysts confined in zeolites. *Chem. Mater.* **2018**, *30*, 3177–3198. [[CrossRef](#)]
4. Aliev, F.A.; Mukhamatdinov, I.I.; Sitnov, S.A.; Ziganshina, M.R.; Onishchenko, Y.V.; Sharifullin, A.V.; Vakhin, A.V. In-situ heavy oil aquathermolysis in the presence of nanodispersed catalysts based on transition metals. *Processes* **2021**, *9*, 127. [[CrossRef](#)]
5. Vakhin, A.V.; Khelkhal, M.A.; Tajik, A.; Gafurov, M.R.; Morozov, O.G.; Nasybullin, A.R.; Karandashov, S.A.; Ponomarev, A.A.; Krapivnitskaia, T.O.; Glyavin, M.Y.; et al. The role of nanodispersed catalysts in microwave application during the development of unconventional hydrocarbon reserves: A review of potential applications. *Processes* **2021**, *9*, 420. [[CrossRef](#)]
6. Franco, F.; Rettenmaier, C.; Jeon, H.S.; Cuenya, B.R. Transition metal-based catalysts for the electrochemical CO_2 reduction: From atoms and molecules to nanostructured materials. *Chem. Soc. Rev.* **2020**, *49*, 6884–6946. [[CrossRef](#)] [[PubMed](#)]
7. van Vreeswijk, S.H.; Weckhuysen, B.M. Emerging analytical methods to characterize zeolite-based materials. *Natl. Sci. Rev.* **2022**, nwac047. [[CrossRef](#)]
8. Saraev, V.V.; Shmidt, F.K. EPR for catalysts based on nickel and cobalt complexes. *J. Mol. Catal. A Chem.* **2000**, *158*, 149–154. [[CrossRef](#)]
9. Xing, Y.; Wang, L.; Yu, H.; Khan, A.; Haq, F.; Zhu, L. Recent progress in preparation of branched polyethylene with nickel, titanium, vanadium and chromium catalytic systems and EPR study of related catalytic systems. *Eur. Polym. J.* **2019**, *121*, 109339. [[CrossRef](#)]
10. Van Doorslaer, S.; Murphy, D.M. EPR spectroscopy in catalysis. *Top. Curr. Chem.* **2011**, *321*, 1–39. [[CrossRef](#)]

11. Morra, E.; Giamello, E.; Chiesa, M. EPR approaches to heterogeneous catalysis. The chemistry of titanium in heterogeneous catalysts and photocatalysts. *J. Magn. Reson.* **2017**, *280*, 89–102. [[CrossRef](#)] [[PubMed](#)]
12. Dyrek, K.; Che, M. EPR as a tool to investigate the transition metal chemistry on oxide surfaces. *Chem. Rev.* **1997**, *97*, 305–332. [[CrossRef](#)] [[PubMed](#)]
13. Brustolon, M.; Giamello, E. *Electron Paramagnetic Resonance: A Practitioners Toolkit*; John Wiley & Sons: Hoboken, NJ, USA, 2009.
14. Mukhambetov, I.N.; Lamberov, A.A.; Yavkin, B.V.; Gafurov, M.R.; Mamin, G.V.; Orlinskii, S.B. Electron paramagnetic resonance and electron nuclear double resonance study of the paramagnetic complexes of anthraquinone on the surface of γ -Al₂O₃. *J. Phys. Chem. C* **2014**, *118*, 14998–15003. [[CrossRef](#)]
15. Eliaz, N.; Metoki, N. Calcium phosphate bioceramics: A review of their history, structure, properties, coating technologies and biomedical applications. *Materials* **2017**, *10*, 334. [[CrossRef](#)]
16. Dorozhkin, S.V. Synthetic Amorphous Calcium Phosphates (ACPs): Preparation, structure, properties, and biomedical applications. *Biomater. Sci.* **2021**, *9*, 7748–7798. [[CrossRef](#)] [[PubMed](#)]
17. Kalinnikova, E.; Sadovnikova, M.; Rodionov, A.; Murzakhanov, F.; Grishin, P. Analysis of the osseointegration process of dental implants by electron paramagnetic resonance: An in vivo study. *Dent. J.* **2022**, *10*, 28. [[CrossRef](#)] [[PubMed](#)]
18. Torres, P.M.C.; Marote, A.; Cerqueira, A.R.; Calado, A.J.; Abrantes, J.C.C.; Olhero, S.; Da Cruz e Silva, O.A.B.; Vieira, S.I.; Ferreira, J.M.F. Injectable MnSr-doped brushite bone cements with improved biological performance. *J. Mater. Chem. B* **2017**, *5*, 2775–2787. [[CrossRef](#)]
19. Monma, H. Catalytic behavior of calcium phosphates for decompositions of 2-propanol and ethanol. *J. Catal.* **1982**, *75*, 200–203. [[CrossRef](#)]
20. Fihri, A.; Len, C.; Varma, R.S.; Solhy, A. Hydroxyapatite: A review of syntheses, structure and applications in heterogeneous catalysis. *Coord. Chem. Rev.* **2017**, *347*, 48–76. [[CrossRef](#)]
21. Goldberg, M.A.; Akopyan, A.V.; Gafurov, M.R.; Makshakova, O.N.; Donskaya, N.O.; Fomin, A.S.; Polikarpova, P.P.; Anisimov, A.V.; Murzakhanov, F.F.; Leonov, A.V.; et al. Iron-doped mesoporous powders of hydroxyapatite as molybdenum-impregnated catalysts for deep oxidative desulfurization of model fuel: Synthesis and experimental and theoretical studies. *J. Phys. Chem. C* **2021**, *125*, 11604–11619. [[CrossRef](#)]
22. Mota, G.; do Carmo, J.V.C.; Paz, C.B.; Saraiva, G.D.; Campos, A.; Duarte, G.; da Silva Filho, E.C.; Oliveira, A.C.; Soares, J.M.; Rodríguez-Castellón, E.; et al. Influence of the metal incorporation into hydroxyapatites on the deactivation behavior of the solids in the esterification of glycerol. *Catalysts* **2022**, *12*, 10. [[CrossRef](#)]
23. Kozłowski, J.T.; Davis, R.J. Heterogeneous catalysts for the guerbet coupling of alcohols. *ACS Catal.* **2013**, *3*, 1588–1600. [[CrossRef](#)]
24. Benarafa, A.; Kacimi, M.; Coudurier, G.; Ziyad, M. Characterisation of the active sites in butan-2-ol dehydrogenation over calcium–copper and calcium–sodium–copper phosphates. *Appl. Catal. A Gen.* **2000**, *196*, 25–35. [[CrossRef](#)]
25. Dikhtyar, Y.Y.; Spassky, D.A.; Morozov, V.A.; Deyneko, D.V.; Belik, A.A.; Baryshnikova, O.V.; Nikiforov, I.V.; Lazoryak, B.I. Site occupancy, luminescence and dielectric properties of β -Ca₃(PO₄)₂-type Ca₈ZnLn(PO₄)₇ host materials. *J. Alloys Compd.* **2022**, *908*, 164521. [[CrossRef](#)]
26. Bessière, A.; Benhamou, R.A.; Wallez, G.; Lecointre, A.; Viana, B. Site occupancy and mechanisms of thermally stimulated luminescence in Ca₉Ln(PO₄)₇ (Ln = lanthanide). *Acta Mater.* **2012**, *60*, 6641–6649. [[CrossRef](#)]
27. Mayer, I.; Cohen, S.; Gdalya, S.; Burghaus, O.; Reinen, D. Crystal structure and EPR study of Mn-doped β -tricalcium phosphate. *Mater. Res. Bull.* **2008**, *43*, 447–452. [[CrossRef](#)]
28. Sinusaite, L.; Renner, A.M.; Schütz, M.B.; Antuzevics, A.; Rogulis, U.; Grigoraviciute-Puroniene, I.; Mathur, S.; Zarkov, A. Effect of Mn doping on the low-temperature synthesis of Tricalcium Phosphate (TCP) polymorphs. *J. Eur. Ceram. Soc.* **2019**, *39*, 3257–3263. [[CrossRef](#)]
29. Khelkhal, M.A.; Eskin, A.A.; Sharifullin, A.V.; Vakhin, A.V. Differential scanning calorimetric study of heavy oil catalytic oxidation in the presence of manganese tallates. *Pet. Sci. Technol.* **2019**, *37*, 1194–1200. [[CrossRef](#)]
30. Ibrahim, M.; Labaki, M.; Nuns, N.; Giraudon, J.-M.; Lamonier, J.-F. Cu–Mn hydroxyapatite materials for toluene total oxidation. *ChemCatChem* **2020**, *12*, 550–560. [[CrossRef](#)]
31. Chlala, D.; Griboval-Constant, A.; Nuns, N.; Giraudon, J.-M.; Labaki, M.; Lamonier, J.-F. Effect of Mn loading onto hydroxyapatite supported Mn catalysts for toluene removal: Contribution of PCA assisted ToF-SIMS. *Catal. Today* **2018**, *307*, 41–47. [[CrossRef](#)]
32. Galukhin, A.; Khelkhal, M.A.; Gerasimov, A.; Biktagirov, T.; Gafurov, M.; Rodionov, A.; Orlinskii, S. Mn-catalyzed oxidation of heavy oil in porous media: Kinetics and some aspects of the mechanism. *Energy Fuels* **2016**, *30*, 7731–7737. [[CrossRef](#)]
33. Sinusaite, L.; Antuzevics, A.; Popov, A.I.; Rogulis, U.; Misevicius, M.; Katelnikovas, A.; Kareiva, A.; Zarkov, A. Synthesis and luminescent properties of Mn-doped alpha-tricalcium phosphate. *Ceram. Int.* **2021**, *47*, 5335–5340. [[CrossRef](#)]
34. Fadeeva, I.V.; Kalita, V.I.; Komlev, D.I.; Radiuk, A.A.; Fomin, A.S.; Davidova, G.A.; Fursova, N.K.; Murzakhanov, F.F.; Gafurov, M.R.; Fosca, M.; et al. In vitro properties of manganese-substituted tricalcium phosphate coatings for titanium biomedical implants deposited by arc plasma. *Materials* **2020**, *13*, 4411. [[CrossRef](#)]
35. Shurtakova, D.V.; Grishin, P.O.; Gafurov, M.R.; Mamin, G.V. Using DFT to calculate the parameters of the crystal field in Mn²⁺ doped hydroxyapatite crystals. *Crystals* **2021**, *11*, 1050. [[CrossRef](#)]
36. Gafurov, M.; Biktagirov, T.; Mamin, G.; Klimashina, E.; Putlayev, V.; Kuznetsova, L.; Orlinskii, S. The interplay of manganese and nitrate in hydroxyapatite nanoparticles as revealed by pulsed EPR and DFT. *Phys. Chem. Chem. Phys.* **2015**, *17*, 20331–20337. [[CrossRef](#)] [[PubMed](#)]

37. Murzakhanov, F.; Mamin, G.V.; Orlinskii, S.; Goldberg, M.; Petrakova, N.V.; Fedotov, A.Y.; Grishin, P.; Gafurov, M.R.; Komlev, V.S. Study of electron–nuclear interactions in doped calcium phosphates by various pulsed EPR spectroscopy techniques. *ACS Omega* **2021**, *6*, 25338–25349. [[CrossRef](#)]
38. Murzakhanov, F.F.; Mamin, G.V.; Goldberg, M.A.; Knotko, A.V.; Gafurov, M.R.; Orlinskii, S.B. EPR of radiation-induced nitrogen centers in hydroxyapatite: New approaches to the study of electron-nuclear interactions. *Russ. J. Coord. Chem.* **2020**, *46*, 729–737. [[CrossRef](#)]
39. Goldfarb, D.; Stoll, S. *EPR Spectroscopy: Fundamentals and Methods*; John Wiley & Sons: Hoboken, NJ, USA, 2018.
40. Yamane, T.; Sugisaki, K.; Matsuoka, H.; Sato, K.; Toyota, K.; Shiomi, D.; Takui, T. ESR analyses of picket fence MnII and 6th ligand coordinated FeIII porphyrins ($S = 5/2$) and a CoII(Hfac) complex ($S = 3/2$) with sizable ZFS parameters revisited: A full spin Hamiltonian approach and quantum chemical calculations. *Dalton Trans.* **2018**, *47*, 16429–16444. [[CrossRef](#)]
41. Rau, J.V.; Fadeeva, I.V.; Fomin, A.S.; Barbaro, K.; Galvano, E.; Ryzhov, A.P.; Murzakhanov, F.; Gafurov, M.; Orlinskii, S.; Antoniac, I.; et al. Sic Parvis Magna: Manganese-substituted tricalcium phosphate and its biophysical properties. *ACS Biomater. Sci. Eng.* **2019**, *5*, 6632–6644. [[CrossRef](#)]
42. Gabbasov, B.; Gafurov, M.; Starshova, A.; Shurtakova, D.; Murzakhanov, F.; Mamin, G.; Orlinskii, S. Conventional, pulsed and high-field electron paramagnetic resonance for studying metal impurities in calcium phosphates of biogenic and synthetic origins. *J. Magn. Magn. Mater.* **2018**, *470*, 109–117. [[CrossRef](#)]
43. Stoll, S.; Schweiger, A. EasySpin, a comprehensive software package for spectral simulation and analysis in EPR. *J. Magn. Reson.* **2006**, *178*, 42–55. [[CrossRef](#)] [[PubMed](#)]
44. Fadeeva, I.V.; Deyneko, D.V.; Barbaro, K.; Davydova, G.A.; Sadovnikova, M.A.; Murzakhanov, F.F.; Fomin, A.S.; Yankova, V.G.; Antoniac, I.V.; Barinov, S.M.; et al. Influence of synthesis conditions on gadolinium-substituted tricalcium phosphate ceramics and its physicochemical, biological, and antibacterial properties. *Nanomaterials* **2022**, *12*, 852. [[CrossRef](#)] [[PubMed](#)]
45. Yashima, M.; Sakai, A.; Kamiyama, T.; Hoshikawa, A. Crystal structure analysis of β -tricalcium phosphate $\text{Ca}_3(\text{PO}_4)_2$ by neutron powder diffraction. *J. Solid State Chem.* **2003**, *175*, 272–277. [[CrossRef](#)]